

			Form Approved OMB NO. 0704-0188	
Public Reporting burden for this collection of information is estimated to average 1 hour per response, including the time for reviewing instructions, searching existing data sources, gathering and maintaining the data needed, and completing and reviewing the collection of information. Send comment regarding this burden estimates or any other aspect of this collection of information, including suggestions for reducing this burden, to Washington Headquarters Services, Directorate for Information Operations and Reports, 1215 Jefferson Davis Highway, Suite 1204, Arlington, VA 22202-4302, and to the Office of Management and Budget, Paperwork Reduction Project (0704-0188,) Washington, DC 20503.				
1. AGENCY USE ONLY (Leave Blank)		2. REPORT DATE 2008-10-31		3. REPORT TYPE AND DATES COVERED Final report
4. TITLE AND SUBTITLE Final Technical Report: Electromagnetic Models for UXO Detection and Classification in Permeable Soils			5. FUNDING NUMBERS W911-NF-05-10384	
6. AUTHOR(S) Beijia Zhang, Jin Au Kong, Kevin O'Neill, Bae-Ian Wu			W911NF-05-1-0384	
7. PERFORMING ORGANIZATION NAME(S) AND ADDRESS(ES) Research Laboratory of Electronics, Massachusetts Institute of Technology, Cambridge, MA 02139, USA			8. PERFORMING ORGANIZATION REPORT NUMBER	
9. SPONSORING / MONITORING AGENCY NAME(S) AND ADDRESS(ES) U. S. Army Research Office P.O. Box 12211 Research Triangle Park, NC 27709-2211			10. SPONSORING / MONITORING AGENCY REPORT NUMBER 49037.1-EV	
11. SUPPLEMENTARY NOTES The views, opinions and/or findings contained in this report are those of the author(s) and should not be construed as an official Department of the Army position, policy or decision, unless so designated by other documentation.				
12 a. DISTRIBUTION / AVAILABILITY STATEMENT Approved for public release; distribution unlimited.			12 b. DISTRIBUTION CODE	
13. ABSTRACT (Maximum 200 words)  Support Vector Machine (SVM) and neural networks (NN), are applied to classifying metallic objects according to size using the expansion coefficients of their magneto-quasistatic (MQS) response in the spheroidal coordinate system. The classified objects include homogeneous spheroids and composite metallic assemblages meant to resemble unexploded ordnance. An analytical model is used to generate the necessary training data for each learning method. SVM and NN are shown to be successful in classifying three different types of objects on the basis of size. They are capable of fast classification, making them suitable for real-time application. Furthermore both methods are robust and have a good tolerance of 20 dB SNR additive Gaussian noise.  We developed a method to convert GEM-3 EMI measurements of unknown units into known quantities. This conversion factor was found through matching modeled responses of spheres to GEM-3 measurements of spheres. Recovery of a soil's susceptibility through GEM-3 measurements via our conversion factor provided validation of our findings. Our results will enable GEM-3 measurements of objects to be directly compared to modeled responses. Furthermore, the conversion factor will enable the magnetic properties of soil to be characterized through in situ measurement conditions.				
14. SUBJECT TERMS Electromagnetic induction, UXO, Differential Evolution, Genetic Algorithm			15. NUMBER OF PAGES 42	
			16. PRICE CODE	
17. SECURITY CLASSIFICATION OR REPORT UNCLASSIFIED	18. SECURITY CLASSIFICATION ON THIS PAGE UNCLASSIFIED	19. SECURITY CLASSIFICATION OF ABSTRACT UNCLASSIFIED	20. LIMITATION OF ABSTRACT	

NSN 7540-01-280-5500

Standard Form 298 (Rev.2-89)  
Prescribed by ANSI Std. Z39-18  
298-102

Enclosure 1

# Final Technical Report: Electromagnetic Models for UXO Detection and Classification in Permeable Soils

Beijia Zhang, Jin Au Kong, Kevin O'Neill, Bae-Ian Wu

March 17, 2008

## Abstract

Two different supervised learning algorithms, Support Vector Machine (SVM) and neural networks (NN), are applied to classifying metallic objects according to size using the expansion coefficients of their magneto-quasistatic (MQS) response in the spheroidal coordinate system. The classified objects include homogeneous spheroids and composite metallic assemblages meant to resemble unexploded ordnance. An analytical model is used to generate the necessary training data for each learning method. SVM and NN are shown to be successful in classifying three different types of objects on the basis of size. They are capable of fast classification, making them suitable for real-time application. Furthermore both methods are robust and have a good tolerance of 20 dB SNR additive Gaussian noise. SVM shows promise in dealing with noise due to uncertainty in the object's position and orientation.

We developed a method to convert GEM-3 EMI measurements of unknown units into known quantities. This conversion factor was found through matching modeled responses of spheres to GEM-3 measurements of spheres. Recovery of a soil's susceptibility through GEM-3 measurements via our conversion factor provided validation of our findings. Our results will enable GEM-3 measurements of objects to be directly compared to modeled responses. Furthermore, the conversion factor will enable the magnetic properties of soil to be characterized through in situ measurement conditions.

# 1 Introduction and Background

Electromagnetic induction (EMI) has been shown to be a promising technique for unexploded ordnance (UXO) detection and discrimination [14, 3]. In this technique, a magneto-quasistatic (MQS) field is transmitted above ground, near the buried object of interest. This field generates currents and possibly magnetic polarization in the target. The induced secondary magnetic fields, also called the scattered fields, are picked up by a receiver. The received signal can then be studied in the time domain or frequency domain to identify buried objects as UXO or to distinguish potential false alarms [6, 13].

The development of UXO discrimination tools requires solving two problems. First, the forward problem requires characterizing, understanding, and examining the EMI response of the various UXO and clutter objects at every permutation of object position and orientation relative to the EMI sensor. Measuring the EMI response so many times is prohibitively expensive. Furthermore, although standard UXO types from the Aberdeen Test Center, U.S. Department of Defense, are known and widely used in research [9, 23], many different types of clutter pieces can be present so it may be difficult to collect enough objects to completely represent the range of clutter items one would expect to see.

Therefore, several increasingly sophisticated forward models have been developed to supply objects' responses under arbitrary excitation [2, 23]. The commonly used dipole model represents the target using an axial and transverse magnetic dipoles. Although this model is sufficient for many cases, it is insufficient as a model for objects close to the sensor. The model also has difficulty capturing the complexities of responses by composite objects. A more sophisticated MQS scattering model is a homogeneous spheroid. Our research team has previously developed an MQS analytical solution for responses by spheroids of arbitrary size, shape, permeability, and electrical conductivity, subject to arbitrary excitation [2, 5, 1]. Prolate or oblate spheroids can accurately represent the responses by surprisingly irregular objects if they are materially homogeneous [21]. Prolate spheroids, in particular, have the elongated body of revolution (BOR) shape common to many UXO. Also, it has been shown that responses from certain types of metallic bodies in very close proximity to one another can be obtained simply by superposing their individual responses [18]. Thus, many types of heterogeneous objects can be modeled by two or more spheroids. These factors motivate the use of combinations of spheroids to construct many examples of materially heterogeneous

objects which more closely resemble many types of UXO.

The second problem that must be solved is the inverse problem: given only the EMI response of an object, we must determine if the object is UXO or clutter. There are several approaches to do this inversion. One method we investigated is the application of a genetic algorithm to search for the appropriate parameters—such as the object’s position and orientation—of a forward model to generate an EMI response that best matches an unknown object’s EMI measurement [29]. This search is repeated for many different modeled objects taken from a library. The closest match between a library object and the measured data will explicitly identify the object, its position, and its location. Although we have shown that this method can successfully identify UXO from measurements, this search is computationally expensive and cannot provide real-time results. Furthermore, this method requires compiling a library of specific possible objects and has difficulty generalizing for objects not included in the library. The method also can suffer from insufficient uniqueness, when optimization procedures forcibly produce similar goodness of fit by disparate objects. Therefore, an alternative method to pursue is to discriminate UXO from clutter. One can solve for general parameters that are properties of an object. These parameters offer clues to the object’s generic features, such as size, shape, and symmetry, which may strongly indicate if the object is UXO or clutter.

One such parameter came to light as the result of our work in developing the spheroidal forward model and the spheroidal coordinate system. This coordinate system is chosen because it most readily conforms to the general shape of objects of interest, thereby requiring the least number of terms in the expansion of the relevant fields. At the same time, responses by any object can be represented in this coordinate system, regardless if it is a body of revolution or not. Within this coordinate system, the excitation and response of a UXO or any other object can be described in terms of scalar spheroidal modes consisting of associated Legendre functions. The spheroidal response modes each have a coefficient  $B_k^j$  which correspond to the  $k$ th mode of the spheroidal response due to the  $j$ th mode of the spheroidal excitation[5]. The  $B_k^j$  have been shown to be unique properties of an object in the sense that objects producing different scattered fields must be characterized by different  $B_k^j$  [6, 5]. For a coordinate system aligned and centered with the target,  $B_k^j$  are completely independent of the excitation, orientation, and location of the object. Thus  $B_k^j$  truly characterize the physical properties of the object. Consequently, the  $B_k^j$  coefficients, which can be recovered from the measured

signal, can be useful as inputs into classification algorithms. However, minimal work has been conducted on the potential of using  $B_k^j$  coefficients for discrimination and classification outside of our research group.

Other UXO recovery and de-mining researchers who are interested in inversion have utilized Bayesian classification, fuzzy systems, and probabilistic neural networks to discriminate objects of interest from clutter [9, 8, 10, 12, 11]. Many of these methods are considered machine learning techniques where algorithms can recognize patterns in the input, such as a UXO's EMI response, to determine a desired output, such as the object's size. Many machine learning techniques like SVM and NN have been shown to be highly capable of dealing with complex and large sets of input values. One popular and successful recent application has been diagnosing hereditary cancer using thousands of genes as input[15]. Since  $B_k^j$  only depends on the object's physical parameters, we propose that the relationship between  $B_k^j$  and the object's physical parameters is both predictable and can be used in the classification of the object as UXO or clutter through the use of machine learning algorithms.

To prove our hypothesis, we first retrieve  $B_k^j$  coefficients from the modeled responses of various single and composite spheroids and then measure the performance of SVM and NN in classifying these objects by object size. The organization of the remainder of this paper is as follows: presentation of key factors that physically differentiate UXO from clutter, motivation for the use of  $B_k^j$ , motivation for the use of machine learning techniques, background on the calculation and retrieval of  $B_k^j$ , introduction to two machine learning techniques, followed by analysis of their performance in classifying various objects based on size. Investigation into the effects of noise will also be presented.

## 2 Background

### 2.1 Background on Spheroidal Mode Coefficients

In active UXO sensing, a primary magnetic field,  $H^{PR}(\vec{r})$ , is transmitted by the sensor. The secondary magnetic field,  $H^S(\vec{r})$ , is the response of the target. In the EMI regime of a few Hz to a few hundred kHz, these magnetic fields can be considered irrotational if the target is embedded in a weakly conducting medium which is usually the case for UXO. Therefore, the primary

and secondary magnetic fields outside of the metallic object can be written in terms of the gradient of a scalar potential:  $U^{PR}(\vec{r})$  for the primary potential and  $U^S(\vec{r})$  for the secondary potential. Furthermore, these two potentials can be expressed as a linear superposition of a finite number of modes, each of which is a solution to Laplace's equation in the particular coordinate system of interest. The spheroidal coordinate system is selected as the basis for this decomposition because, as mentioned before, UXO tend to have a somewhat elongated spheroidal shape. Therefore accurate representation of UXO responses can be achieved without needing to use too many modes. In this coordinate system, the potentials are written as:

$$U^{PR}(\vec{r}) = \frac{d}{2} \sum_{m=0}^{\infty} \sum_{n=m}^{\infty} \sum_{p=0}^1 b_{pmn} P_n^m(\eta) P_n^m(\xi) T_{pm}(\phi) \quad (1)$$

$$U^S(\vec{r}) = \frac{d}{2} \sum_{m=0}^{\infty} \sum_{n=m}^{\infty} \sum_{p=0}^1 B_{pmn} P_n^m(\eta) Q_n^m(\xi) T_{pm}(\phi) \quad (2)$$

$$T_{pm}(\phi) = \begin{cases} \cos(m\phi) & p = 0 \\ \sin(m\phi) & p = 1. \end{cases} \quad (3)$$

where  $\vec{r}$  refers to the observation location. Coordinates are defined in terms of  $\eta$  which indicates a spheroidal surface, and  $\xi$  and  $\phi$  which describe the azimuthal and rotational positions, respectively. In equations 1 and 2,  $P_n^m()$  and  $Q_n^m()$  are the associated Legendre functions of the first and second kind, respectively. The parameter  $d$  is the interfocal distance of the spheroidal coordinate system in use. The different permutations of the summation indices  $(p, m, n)$  distinguish the different modes of the equations. For the sake of compactness, we can write  $(p, m, n)$  using one index, each value of which corresponds to one permissible combination of  $p$ ,  $m$ , and  $n$ . Thus, index  $j$  is used for the primary potential, and the index  $k$  is similarly used for the secondary potential. Furthermore, we can represent the associated Legendre functions and  $T_{pm}$  using the symbols  $\Psi_j^{PR}$  in equation 1 and  $\Psi_k^S$  in equation 2. Using this notation, equations 1 and 2 become equations 4 and 5, respectively:

$$U^{PR}(\vec{r}) = \frac{d}{2} \sum_j b_j \Psi_j^{PR}(\vec{r}) \quad (4)$$

$$U^S(\vec{r}) = \frac{d}{2} \sum_k B_k \Psi_k^S(\vec{r}). \quad (5)$$

The primary and secondary magnetic fields that can be obtained by taking the gradient of equations 1 and 2:

$$\vec{H}^{PR}(\vec{r}) = \frac{-d}{2} \sum_j b_j \nabla \Psi_j^{PR}(\vec{r}) \quad (6)$$

$$\vec{H}^S(\vec{r}) = \frac{-d}{2} \sum_k B_k \nabla \Psi_k^S(\vec{r}) \quad (7)$$

$$\vec{H}^S(\vec{r}) = \sum_j b_j \vec{H}_j^S(\vec{r}) = \sum_j b_j \frac{-d}{2} \sum_k B_k^j \nabla \Psi_k^S(\vec{r}). \quad (8)$$

$\vec{H}_j^S$  represents the secondary field response to a single excitation mode  $j$ . We can decompose  $\vec{H}_j^S$  in the same manner as done for  $\vec{H}^S$  in equation 7 to obtain the  $B_k^j$  coefficients in equation 8. These coefficients correspond to the  $k$ th mode of the spheroidal response to the  $j$ th mode of the spheroidal excitation. They are independent of particular primary excitation used. Furthermore, all position and orientation effects are encompassed by  $\nabla \Psi_k^S$ . As a result, for any specific spheroidal coordinate system defined with  $d$ , axis orientation, and a chosen origin, the  $B_k^j$  only depend on the physical properties of the scattering object. In addition, it can be rigorously mathematically proven that all objects with unique EMI responses also have unique  $B_k^j$  coefficients [1, 2].

## 2.2 Background on Learning Machines

As we have stated, determining whether an object is clutter or a UXO by using the  $B_k^j$  coefficients of the object requires an understanding of the patterns in the coefficients which give clues about the nature of the object. Supervised learning machines excel in the field of pattern identification. The basic idea behind learning machines is that given a set of  $l$  observations, consisting of an input vectors  $x_i \in R^n, i = 1, \dots, l$  and the associated truth  $y_i$ , the learning machine finds the right mapping  $x_i \rightarrow y_i$ .

When one “trains” a learning machine, one is finding the correcting mapping. The initial set of  $x_i$  and  $y_i$  input vectors are appropriately named the “training data.” The performance of a trained machine can be evaluated with a set of new  $x$  test data for which the machine must perform the mapping. The correct associated  $y$  is withheld from the machine. The  $y$  that is found through the mapping is then compared to the true  $y$  for accuracy. A

machine is over-trained if it is only able to recognize and produce the correct output for  $x$  that are extremely similar to or even exactly like members of the training data. This scenario creates a machine that inaccurate for noisy data or slightly different input cases. On the other hand, an under-trained machine is simply too general and does not recognize enough of the specific underlying pattern in the data, leaving it unable to correctly classify test examples. An ideal machine is capable of generalizing and finding the accurate outputs for a very broad range of inputs.

For our purposes the output  $y_i$  is a binary value, being either -1 or +1, representing the two possible classes: large and small objects. Thus our problem is a binary classification problem. We consider each input vector  $x_i$  to be the set of  $B_k^j$  for an object. This type of training data is given to two well known machine learning algorithms, SVM and NN.

### 2.2.1 Background on SVM and mySVM

SVM is a form of machine learning where each input vector  $x_i$  is a point that is mapped into an  $n$ -dimensional space with  $n$  being the length of the vector. The basic objective of an SVM is to find the optimal hyperplane that correctly separates the points of the two classes as completely as possible. When a test vector is presented, a trained SVM only has to find on which side of the hyperplane the new point falls to determine its class. Therefore, the classification process is normally very fast, making it attractive for our purposes. A constraint is that SVM can normally only do binary classification. For further explanation of SVM, the reader is directed to reference [26].

We use mySVM, a freely distributed implementation of SVM based on SVMLight [16, 26]. For our experiments mySVM operates in its “pattern matching” mode with a radial kernel function. Training of mySVM is very quick, converging in less than a minute for a 1800 member training set on a 3.6 GHz Pentium 4 machine with 3.5 GB of memory. mySVM automatically finds the ideal balance between overtraining and undertraining.

### 2.2.2 Background on Neural Networks

A NN consists of a collection of interconnected processing elements, called “neurons” to collectively perform the  $x_i \rightarrow y_i$  transformation. The neurons each have an input and output with a transfer function and a bias. The



neurons are organized into layers with outputs of one layer interconnected to the inputs of the subsequent layer. The output of the last layer form the desired  $y_i$ . The connections between the neurons have an associated weight. The biases of all the neurons and all these weights are incrementally adjusted during training to find the correct mapping function. Like SVM, a trained NN is very fast in finding the output for a given input.

The adjustment and training process requires in-depth explanation and readers are provided with references [27, 4]. A great concern, however, is that a NN may be over-trained. Cross validation and limiting the training cycles helps to prevent over-training. An overly complex network with too many weights make cause the algorithm to be erratic and unreliable. The final architecture is highly dependent on the nature of the input data. Therefore, starting with a very simple network and then adding more neurons until low error on the training data and good cross validation performance is achieved is one method to obtain a reliable network [27].

### 2.3 Implementation of a Neural Network

Unlike mySVM which was developed elsewhere, the NN we use in this study is developed by the authors. We use Matlab's NN toolbox to efficiently implement a three hidden layer feed forward NN. All nodes have a tan-sigmoid transfer function except the final output node which is a linear transfer function. The weights and biases of the network are initialized with random values, taken from -1 to 1. We choose to use batch training where the weights between the nodes are updated only after all the training examples have been exposed to the network. We use Levenberg-Marquardt back-propagation when training and find in practice that this method gives the best results. This type of training requires more memory but is comparatively faster than other common training methods. Even so, training our NN is much slower than training the SVM. Where the SVM takes under a minute with 1800 training objects, the NN takes close to 10 minutes using the same computer. However, after both algorithms are trained, both methods can classify objects nearly instantaneously, permitting them to be potential candidates for real time classification.

One significant feature of our NN is that the inital weights and biases are random. Therefore, separate attempts to train with the same data will produce realizations of networks that have differing classification ability. In our experience, using a larger number of training samples minimizes the

possibility of having an inaccurate NN due to unfortunate initial weights and biases.

### 3 Data Collection and Generation

#### 3.1 Retrieval of $B_k^j$ from Magnetic Fields

As mentioned earlier, the successful recovery of  $B_k^j$  is not the focus of our research. However, it is beneficial to understand the general framework by which we obtain the  $B_k^j$  used in our study. The  $B_k^j$  for an object can be obtained through two basic methods: 1) match boundary conditions and find the solution analytically and 2) understand that equation 8 is a system of linear equations in  $B_k^j$  when several observation positions are of interest so it is possible to invert for  $B_k^j$  using a calculated or measured magnetic fields at those points. The first method is difficult and possible for only canonical shapes. It cannot be applied in a realistic UXO clean-up scenario. So consequently, we obtain the  $B_k^j$  using the second method. The  $B_k^j$  in this study are synthetic in the sense that they were recovered from magnetic fields generated from a forward model. The  $B_k^j$  are recovered from the magnetic fields at 578 points in space, thus ensuring the problem is overdetermined. These points were distributed over a 2 m by 2 m grid at two elevations. Figure 1 gives a graphical depiction of this arrangement. Furthermore, as mentioned earlier, we follow the Tikhonov regularization methods of [7] to ensure our recovered  $B_k^j$  values are accurate.

We use only the 7 lowest order excitation modes and 4 lowest response modes, giving a total of 28  $B_k^j$  coefficients. Previous work demonstrated that these low order modes dominate the solution and are sufficient to reproduce it [6]. The modes  $(0, 1, 1)$ ,  $(1, 1, 1)$ , and  $(0, 0, 1)$  for  $k$  correspond to the magnetic dipole moments in  $x, y$ , and  $z$  directions for each excitation mode. Thus for each  $j$ , we are only solving for one more mode, the lowest order mode, in addition to the three modes which correspond to the triaxial dipole moments. Each  $B_k^j$  is a complex value. But due to the limitations of the SVM algorithm, the real and imaginary parts are considered as independent inputs when processing. For each object, we consider the  $B_k^j$  at two frequencies: one high at 10950 Hz and one low at 210 Hz. This choice of frequencies is due to the nature of the EMI response: these frequency extremes can capture the largest variation in an object's Inphase frequency

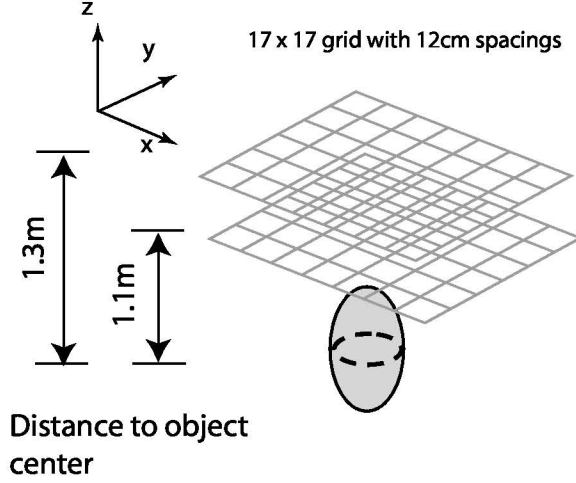


Figure 1: Diagram of the measurement locations used in the inversion process.

response. Consequently, we have a vector of total length  $n = 112$  as input for each object into the SVM and the NN.

The method of obtaining  $B_k^j$  from the magnetic fields can be applied to both measured data and data from a forward model that gives the EMI response of various objects. However, it should be mentioned that while test data can be obtained through measurements, training data will likely always be largely from synthetic data. If the training data is too sparse, it may not capture enough of the trends in the  $B_k^j$  for SVM and NNs to do reliable prediction. Therefore, it is advantageous to have larger sets of training data. However, it is usually not feasible to obtain enough measured data to create a large training data set. Some previous work included a few instances of real measurements in the training data, but the training data was still largely composed of synthetic data [6].

Though subsequent sections will describe how we create synthetic data using forward models, the particulars of how these objects are modeled are distinct from our investigation into the validity of using  $B_k^j$  for classification purposes. For example, we can model an object at 20cm below the sensor level or 30cm below. We could even chose random values for depth. But in the object-centered spheroidal coordinate system, the  $B_k^j$  are entirely independent of the actual position and orientation of the objects. It may be more difficult to recover enough  $B_k^j$  when the object is positioned at a greater dis-

tance from the sensor. However, we are only recovering the lowest modes, and recovery of accurate  $B_k^j$  at reasonable depths has already been shown to be possible [7]. While it is true that we must know the actual location of objects to create the object-centered spheroidal coordinate system, this data can come from complementary techniques such as GPR. Furthermore, we also show in subsequent sections that our methods are robust enough to cope with a significant level of uncertainty in the object’s position and orientation.

### 3.1.1 Object Geometry and Composition

For our investigation, we use three different object types. First, the simplest object is a single spheroid as shown in Figure 2(a). The spheroid has two possible permeability and conductivity values: either  $\mu_r = 100$  with  $\sigma = 2 \cdot 10^6 S/m$  or  $\mu_r = 1$  with  $\sigma = 2 \cdot 10^7 S/m$ . These values approximate steel and aluminum, two metals commonly present in UXO and clutter. The elongation of each spheroid, the ratio of major axis length to minor axis length, is taken from a uniform distribution ranging from 0.1 to 4. The volume is likewise random and uniformly distributed, ranging from  $0.001m^3$  to  $0.08m^3$ .  $0.04m^3$  is the cutoff between “large” and “small” objects. This range of values corresponds to the variety of UXO and clutter objects we expect to encounter in the field. If different ranges of volumes are of interest, both learning algorithms can be trained to recognize different cutoff values. These spheroids are modeled using a previously implemented algorithm [2]. This method can calculate the magnetic field response of any spheroid of arbitrary shape, size, permeability, conductivity and in response to any arbitrary excitation. The main obstacle in the generation of synthetic data is the amount of time needed to create enough objects for the training set. To generate data for 1800 objects, around two days are needed on a 3.6 GHz Pentium 4 PC.

The second type of object we can model is a heterogeneous object composed of two small spheroids that are coaxial and are separated by a distance of 1mm as shown in in Figure 2(b). We refer to this composite object as a BOR composite object. This object is always positioned so that the gap is fixed at the center of the coordinate system. The two spheroids that form a composite object are always given two different permeability and conductivity values:  $\mu_r = 100$  with  $\sigma = 2 \cdot 10^6 S/m$  and  $\mu_r = 1$  with  $\sigma = 2 \cdot 10^7 S/m$ . The elongation of each spheroid is again random. The total volume of both

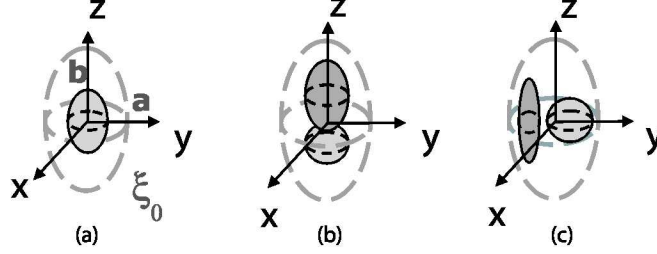


Figure 2: Three different configurations of spheroids: single, BOR composite, and non-BOR composite. The  $B_k^j$  of these three objects are used for SVM and NN training and testing.

spheroids ranged from  $0.001m^3$  to  $0.08m^3$ . To obtain the response of a composite object, the magnetic field response of each spheroid is independently calculated and then summed. Therefore, we assume that the interaction between the two spheroids do not affect the fields at the observation points which are at least a characteristic length away. Prior analysis has shown that this is a reasonable assumption even when the two objects are closely spaced as long as one object is not permeable [18].

The third type of object under study is shown in Figure 2(c). This object is similar to the BOR composite object except now the axes are parallel to each other and the  $z$ -axis. The gap between the two spheroids is again 1mm and is positioned at the center of the coordinate system. We refer to this object as a non-BOR composite object.

The excitation is described by a model of the GEM-3 sensor [22]. The GEM-3 instrument, the primary tool in our EMI measurements, is manufactured by Geophex [28]. This instrument consists of two current loop in a bucking coil arrangement to generated primary magnetic field. The secondary magnetic field is captured by the current generated on a pickup coil in the center of the instrument by  $\partial B/\partial t$ . The instrument reports this current in units that are proportional to the integral of magnetic flux over the reciever coil.

## 4 SVM Classification Performance

For all tests, the training data is a set of 1800 objects that are evenly divided into the two possible classes of large and small. The test data set has 200

Table 1: Confusion Matrix for SVM Classification of Single Objects

	True Large	True Small
Predicted Large	99	1
Predicted Small	1	99

members and is generated independently from the training data set. Adequate classification can be achieved with as few as 600 training examples for the simple case of single spheroid test objects with no additive noise. However, in our experience, the more complex objects presented in the subsequent sections require larger training sets to be optimally classified. Therefore, to permit reasonable comparison of the classification performance for different objects, all training sets have 1800 members. Many classification studies employ small training sets and larger test sets because the training sets, often derived from measurements and collected data, are difficult to obtain. However, our forward model can provide large amounts of training data within a reasonable amount of time. Also, in our experience a 200 member test set is sufficiently large enough to provide an accurate gauge of performance.

In our first test, when single objects are classified by a trained SVM, only 2 objects are misclassified. Table 1 is the confusion matrix that of the result of classifying the test data. SVM misclassifies 2 objects out of a total of 200, yielding an error of 1%. We choose to use this error as the overall figure of merit as opposed to separate false positive and false negative rates. We identify the members of the test data by assigned classification in the scatter plot shown in Figure 3. The horizontal axis of this plot is a rough metric for overall size of  $B_k^j$  while the vertical axis is the actual volume of the object. The errors made by SVM are concentrated close to the boundary between “large” and “small.” While the clustering of markers suggests some correlation between object size and overall  $B_k^j$  magnitude, the relationship is not strict as we have discussed earlier. One can clearly see many large objects with lower  $B_k^j$  than smaller objects and visa versa. We expect the distribution of  $B_k^j$  magnitude as a function of object size to be even more random when we extend our study to cover additional permeability and conductivity values.

Furthermore, our decision to use 28  $B_k^j$  coefficients for each object comes about after examining the error rates due to using more or fewer coefficients

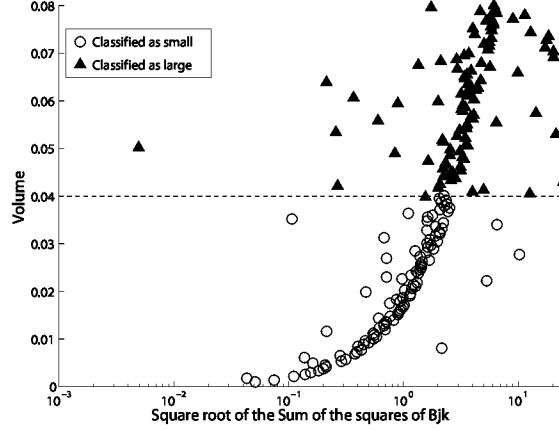


Figure 3: Scatter plot for SVM classification of single objects. Each marker represents one object, plotted against its corresponding true volume and  $B_k^j$  magnitude. The marker’s face is determined by its class as predicted by SVM. The horizontal dotted line represents the boundary between large and small objects.

Table 2: SVM Classification of Single Objects Using Various Number of Coefficients

	16 $B_k^j$	28 $B_k^j$	42 $B_k^j$
<b>Percent Error</b>	9.5%	1.0%	2.5%

when classifying 200 single spheroid objects as shown in Table 2. We aim to use the fewest lowest order  $B_k^j$  coefficients that would still give good results. Recovering higher order  $B_k^j$  is likely to cause ill-conditioning and produce unreliable data. This problem becomes even more apparent when recovering  $B_k^j$  from measured data [6]. However, using too few coefficients did not encapsulate enough information about the object and can also lead to high classification error.

Table 3 shows how SVM is able to generalize for different types of objects. We have three sets of test data and three sets of training data. These three sets correspond to the three different types of objects as shown in figure 2. All cases use 200 test objects and 1800 training objects. The lowest errors

Table 3: Table of Error for SVM Classification with Different Training and Testing Sets

	<b>Train: Single (BOR)</b>	<b>Train: Compos- ite (BOR)</b>	<b>Train: Compos- ite (non- BOR)</b>
<b>Test: Single</b>	1.00%	24.0%	50.0%
<b>Test: Compos- ite (BOR)</b>	18.5%	3.00%	47.5%
<b>Test: Compos- ite (non-BOR)</b>	50.0%	50.0%	1.50%

are generated when we train and test using the same type of object. When SVM is trained on single spheroids and tested on BOR composite objects or visa versa, it is able to generalize across these two object types to a certain degree. But it has difficulty classifying non-BOR objects when trained on any of the other two types or visa versa. In many cases an exact 50% error is obtained when SVM simply classified all objects as large or all objects as small. This unsuccessful classification may be due to the peculiarity of BOR objects in that they have values of zero for many specific  $B_k^j$  coefficients while non-BOR objects do not have this constraint [6]. Due to this very distinct difference in pattern, we expect SVM to have greater difficulty when generalizing across BOR and non-BOR objects.

However, when SVM is given sufficient training data, it can adequately classify all objects. Table 4 shows the effects of training on a combination of single and BOR composite objects and a combination of all three types of objects. Remarkably, training on a combination of BOR composite and single objects allows SVM to be even more accurate in classifying BOR type objects. Furthermore, training with all three object types creates a more general SVM that can classify all objects with under 5% error.

For any classification technique to be of practical use, it must be able to generalize for a wide range of objects. Thus, this use of dissimilar training and testing objects characterizes the generalizability of each trained learning method. Furthermore, mixed training sets, comprised of two or more types of objects, helps to illustrate how broadening the scope of the training sets



Table 4: Table of Error for SVM Classification with Mixed Training Sets

	<b>Train: Single and Compos- ite (BOR)</b>	<b>Train: All Three Types</b>
<b>Test: Single</b>	1.00%	2.50%
<b>Test: Compos- ite (BOR)</b>	0.00%	4.50%
<b>Test: Compos- ite (non-BOR)</b>	50.0%	4.50%

Table 5: Confusion Matrix for Neural Network Classification

	<b>True Large</b>	<b>True Small</b>
<b>Predicted Large</b>	99	0
<b>Predicted Small</b>	1	100

improves generalizability and leads to overall robustness.

## 5 Neural Network Classification Performance

All the training and test data that are used to generate the results for SVM are also used for training and testing our NN. Table 5 and Figure 4 show that the NN was able to achieve comparable and perhaps even slightly better results when compared to the SVM results for single spheroid classification.

Table 6 shows how well the NN is able to generalize for different objects. The NN has more difficulty generalizing for a test object type that differs from the training object type. While SVM trained on single objects produces an error rate of 18.5% when tested with composite objects, this error is significantly larger when the NN processes the same data. This suggests that our current NN has somewhat less ability to generalize between the single spheroid objects and the composite BOR object. However, once the NN is trained with all three types of objects, it is able to correctly classify all objects with low error as shown in Table 6

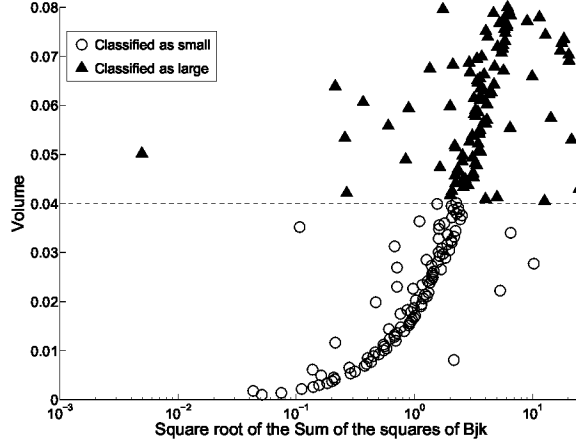


Figure 4: Scatter plot for NN classification of single objects. Each marker represents one object, plotted against its corresponding true volume and  $B_k^j$  magnitude. The marker's face is determined by its class as predicted by NN. The horizontal dotted line represents the boundary between large and small objects.

Table 6: Table of Error for NN Classification with Different Training and Testing Sets

	Train: Single (BOR)	Train: Com- posite (BOR)	Train: Com- posite (non- BOR)
Test: Single	0.500%	41.0%	50.5%
Test: BOR Composite	28.5%	1.50%	48.5%
Test: non- BOR Com- posite	49.0%	47.5%	3.50%

Table 7: Table of Error for NN Classification with Mixed Training Sets

	<b>Train: Single and Com- posite (BOR)</b>	<b>Train: All Three Types</b>
<b>Test: Single</b>	0.500%	1.50%
<b>Test: BOR Composite</b>	1.00%	3.00%
<b>Test: non-BOR Composite</b>	51.0%	2.00%

## 6 Effect of Additive Gaussian Noise

As mentioned earlier, using dissimilar training objects from test objects is done to understand the limitations of each trained learning algorithm when exposed to entirely foreign objects. The wide variety of clutter objects and UXO makes understanding and minimizing this limitation absolutely necessary for any classification technique to be of practical use. Another realistic obstacle to accurate classification is the effect of noise. This noise can be in the form of additive instrument and environmental noise which corrupts the received magnetic field which in turn lead to small changes in the retrieved  $B_k^j$ . The relationship between the amount of change in seen  $B_k^j$  and the amount of noise in the EMI signal has already been investigated. Despite an addition of Gaussian noise that is 10% of the true field strength,  $B_k^j$  can be recovered accurately: for secondary responses at new measurement points, there is less than a 10% error between the direct prediction by forward models and the calculation from the recovered  $B_k^j$  [6, 7]. For this investigation, it is then necessary for us to study how much that small change in  $B_k^j$  affects our classification ability.

For our purposes, we define noise in terms of SNR, using additive Gaussian noise of 20dB SNR as an estimate of light background and instrument

Table 8: Table of Error for SVM Single Object with Noise

	<b>Train: No Noise</b>	<b>Train: 20dB SNR</b>	<b>Train: No Noise and 20dB SNR</b>
<b>Test: No Noise</b>	1.00%	4.00%	5.50%
<b>Test: 20dB SNR</b>	25.0%	8.50%	11.5%

noise. From the noisy H fields, the retrieved  $B_k^j$  are then given to both the SVM and the NN. For this study, we limit our investigation of additive noise effects to only single spheroid objects. The performance is outlined in Tables 8 and 9. Since our goal is to have both an SVM and a NN that can generalize for noisy data, we train both with noisy and clean training data and then test each against noisy and clean test data. From the results it seems both NN and SVM have difficulty classifying noisy data if they are only trained on clean data. However, both methods have considerably lower error once they are trained on noisy data. NN is able to provide lower error rates compared to SVM. Furthermore, training on noisy data does not cause NN to have any significant change in error rate when classifying clean data. Both methods show no further improvement if they are trained on both noisy and clean data. The effect of this training is confirmed when repeated on BOR and non-BOR composite objects as shown in Tables 10 and 11. Classification is much more difficult for composite objects. We speculate that this phenomenon is due, in part, to the heavier reliance of the EMI response on higher order modes which are more difficult to recover accurately from noisy signals.

Table 9: Table of Error for NN Single Object with Noise

	<b>Train: No Noise</b>	<b>Train: 20dB SNR</b>	<b>Train: No Noise and 20dB SNR</b>
<b>Test: No Noise</b>	0.500%	2.50%	2.00%
<b>Test: 20dB SNR</b>	24.0%	5.50%	5.00%

Table 10: Table of Error for Classification of BOR Composite with Noise

	<b>SVM Train: 20dB SNR</b>	<b>NN Train: 20dB SNR</b>
<b>Test: No Noise</b>	14.00%	9.50%
<b>Test: 20dB SNR</b>	17.00%	12.50%

Table 11: Table of Error for Classification of Non-BOR Composite with Noise

	<b>SVM Train: 20dB SNR</b>	<b>NN Train: 20dB SNR</b>
<b>Test: No Noise</b>	17.00%	12.00%
<b>Test: 20dB SNR</b>	20.50%	15.50%

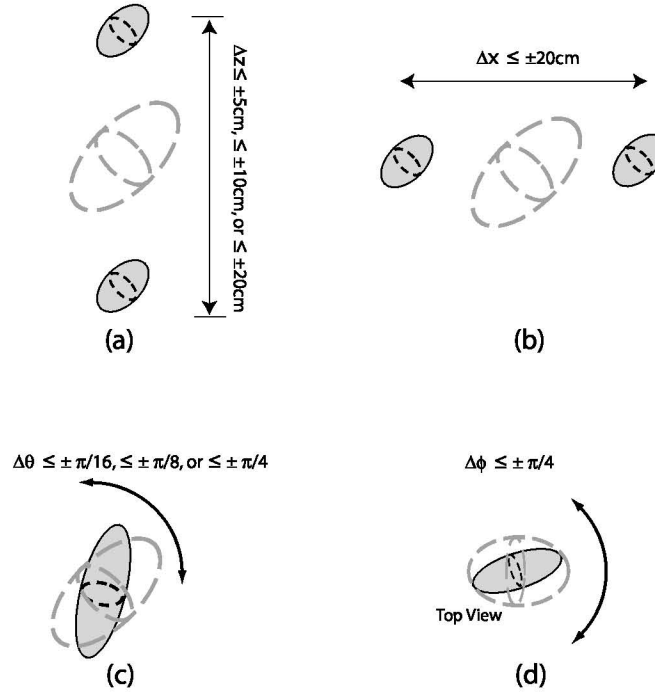


Figure 5: Figure showing the bounds on (a)  $z$  variation, (b)  $x$  variation, (c)  $\theta$  variation, and (d)  $\phi$  variation in the study on position and orientation uncertainty. All objects have random volumes, dimensions, and material properties.

## 7 Effect of Position Noise

In the previous simulations, all objects were at fixed positions and aligned with the coordinate system. This arrangement, however, does not reflect real life situations where there may be uncertainties about the exact locations of buried objects. It is therefore more realistic to estimate the location of an object and center our spheroidal coordinate system near the true center point. This uncertainty will introduce noise into the recovered  $B_k^j$  coefficients. To study the effects of that noise, we recover the  $B_k^j$  from single spheroids which have four types of misalignments in position and orientation from the origin and orientation of our assumed coordinate system: depth deviation in  $z$ , lateral deviation in  $x$ , rotational deviation in  $\theta$ , and rotational deviation in  $\phi$ . These four types are summarized in Figure 5. The volumes and material properties of the objects are otherwise similar to our previous cases of single spheroids. From the modeled data, the  $B_k^j$  are inverted using an assumed coordinate system that is misaligned by a specified deviation. The deviation is generated randomly using a uniform distribution. Both training and test data are generated in this manner.

For  $z$  variation, the centers of the spheroids are allowed to vary within a  $\pm 5$  cm range of random deviation (up to 5 cm below and above the center of the assumed coordinate system), a  $\pm 10$  cm range of random deviation, or a  $\pm 20$  cm range of random deviation, as depicted in Figure 5 (a). The object and the coordinate system are kept at a fixed  $\theta$  angle of  $\pi/4$  and a fixed  $\phi$  angle of 0. Table 12 reports the errors for different combinations of testing and training data. Like in the additive Gaussian noise cases, training with noisy data improves SVM’s ability to classify noisy test data. We see that our method tolerates a  $\pm 5$ cm variation quite well with under 10% error when we use noisy training data drawn from either the  $\pm 5$ cm and  $\pm 10$ cm ranges. When the training data is drawn from the  $\pm 5$ cm range, our methods can obtain an under 10% error for  $\pm 10$ cm range test data. An uncertainty of  $\pm 20$ cm in either the training or the test data creates significantly less accurate results.

Next, we examine the effect of lateral deviation. Here the objects are permitted up to a  $\pm 20$  cm deviation in the  $x$  direction from the fixed center of the coordinate system. The object and the coordinate system are kept at a fixed  $\theta$  angle of  $\pi/4$  and a fixed  $\phi$  angle of 0. This arrangement is depicted in Figure 5 (b). From Table 13, we see that a large lateral uncertainty has a much smaller effect than an equally large vertical uncertainty.

Table 12: Table of Error for SVM with Z Position Deviation

	<b>Train: No Devia- tion</b>	<b>Train: <math>\pm 5\text{cm}</math> Devia- tion</b>	<b>Train: <math>\pm 10\text{cm}</math> Devia- tion</b>	<b>Train: <math>\pm 20\text{cm}</math> Devia- tion</b>
<b>Test: No Deviation</b>	1.00%	2.00%	2.00%	7.00%
<b>Test: <math>\pm 5\text{cm}</math> Deviation</b>	12.0%	1.50%	3.50%	38.0%
<b>Test: <math>\pm 10\text{cm}</math> Deviation</b>	46.0%	7.50%	10.5%	21.5%
<b>Test: <math>\pm 20\text{cm}</math> Deviation</b>	44.0%	22.0%	16.0%	36.0%

Table 13: Confusion Matrix for SVM Classification of X Position Deviation 20 cm

	<b>True Large</b>	<b>True Small</b>
<b>Predicted Large</b>	96	4
<b>Predicted Small</b>	4	96



Table 14: Table of Error for SVM with  $\theta$  Orientation Deviation

	<b>Train: No De- viation</b>	<b>Train: <math>\pm\pi/16</math> Devia- tion</b>	<b>Train: <math>\pm\pi/8</math> Devia- tion</b>	<b>Train: <math>\pm\pi/4</math> Devia- tion</b>
<b>Test: No Deviation</b>	1.00%	1.00%	3.50%	4.50%
<b>Test: <math>\pm\pi/16</math> Deviation</b>	2.00%	2.00%	1.50%	3.00%
<b>Test: <math>\pm\pi/8</math> Deviation</b>	1.50%	7.00%	1.50%	4.50%
<b>Test: <math>\pm\pi/4</math> Deviation</b>	4.50%	4.50%	4.00%	6.00%

The third type of variation concerns object orientation. The coordinate system is oriented at  $\theta = \pi/4$  but the object's  $\theta$  is permitted to vary up to  $\pm\pi/16$ ,  $\pm\pi/8$ , and  $\pm\pi/4$  from  $\pi/4$ . The  $\phi$  angle is fixed at 0. This arrangement is depicted in Figure 5 (c). Table 14 shows that variation in  $\theta$  orientation does not have a significant impact on the classification accuracy.

The final type of variation concerns object orientation in the  $\phi$  direction. The coordinate system is oriented at  $\phi = 0$  but the object's  $\phi$  is permitted to vary up to  $\pm\pi/4$  from 0. The  $\theta$  angle is fixed at  $\pi/4$ . This arrangement is depicted in Figure 5 (d). Table 15 shows that variation in  $\phi$  orientation creates a classification error of 6.5% which is on par with the  $\theta$  variation scenarios. The classification errors for all orientation variations are under 10%.

We can understand these results from an intuitive perspective. The magnitude of the response from a small object at a very shallow depth can be equal to or greater than the response of a larger, more deeply buried object. While there will be differences between these two responses across a frequency spectrum, our use of very low order  $B_k^j$  at only two frequencies may not completely characterize this difference though the sets of recovered

Table 15: Confusion Matrix for SVM Classification of  $\phi$  Orientation Deviation

	True Large	True Small
Predicted Large	87	0
Predicted Small	13	100

$B_k^j$  coefficients are dissimilar. The poor classification performance on these types of data suggests the ambiguity created by the incomplete characterization is beyond acceptable limits. Lateral shifts and rotation, in contrast, would not normally introduce a great change the overall magnitude of the response. Our methods retain their level of accuracy if given appropriate training data. Testing of composite objects and of objects that have vertical, lateral, and orientation uncertainties in combination will be a future goal.

Furthermore, these results are applicable in the research of recovering of UXO’s location and orientation. These results suggest that a depth accuracy of under 10 cm should be achieved to create a viable solution for UXO discrimination. In addition, these results indicate that the larger effort should be placed in accurately resolving an object’s depth rather than finding an object’s orientation and  $x - y$  location with great precision. We hope to confirm these ideas through the application of Neural Networks on our testing and training objects.

## 8 Conclusion

In this paper the problem of classification by volumetric size of metallic objects using their EMI response is solved by decomposing that response into  $B_k^j$  coefficients and then using a SVM and a NN to process those coefficients. The performance of each method is compared. Since we demonstrate that there is no simple relationship between sizes of objects and the overall magnitude of their  $B_k^j$  coefficients, learning algorithms are necessary and useful in classifying these objects. Furthermore, both learning algorithms are able to generalize for different object types with varying degrees of success. Both algorithms are capable of classifying single objects when trained on BOR composite objects or visa versa. However, both have difficulty classifying non-BOR objects when trained on any of the other two types or visa versa.

We believe that this increased error is due to the single spheroid also being BOR so the non-BOR objects are very different from the other two types. When trained on all three types of objects, both the NN and the SVM are able to classify all objects with a good degree of accuracy.

In addition, both methods show an ability to generalize for noisy test data when trained with noisy data. This noise can be in the form of additive Gaussian noise or small variations in the position or orientation of the objects relative to the coordinate system. Training on noisy data helps to increase the accuracy of both learning algorithms when classifying objects with noisy  $B_k^j$ . For additive gaussian noise, the NN proves to be slightly more accurate. In the preliminary analysis on the effects of uncertainty in object position and orientation, we see that large deviations in an object's depth can significantly decrease the SVM classification accuracy. Since accuracy with noisy measured data is very critical for any classification method to be viable in the field, we believe training using data with added noise and uncertainty makes our method closer to providing a realistic, practical solution to the difficult problem of UXO discrimination.

Furthermore, there is a possibility of developing this technique into a real time application. Training each learning method is not instantaneous but not excessively time consuming for the two algorithms we have studied. Once a learning algorithm is trained, it can be used for an extended period of time until the user feels more accurate training data is available. Generating synthetic test data is the most time consuming part of our research, but this data can be stored and used indefinitely. The actual classification of test data by SVM or NN is nearly instantaneous. Solving for the appropriate  $B_k^j$  from measurements is also nearly instantaneous. Therefore, classification of a buried object as UXO or a piece of clutter can theoretically be obtained as quickly as the EMI measurements can be completed when the object position and orientation are known. The technique presented in this paper can be supplemented by other methods to obtain that data.

We believe that our NN model can be further refined and produce even more accurate results in the future. In addition, we are interested in writing our own SVM program that will be better adapted to handling  $B_k^j$  data since the current implementation treats complex inputs as two separate, independent inputs. We anticipate augmenting our test objects with other more complicated objects such as spheroids in different configurations or have components that are other shapes. We have not yet attempted to classify composite objects with uncertainty in object position and orientation.

We have also not yet applied NN on objects with position and orientation uncertainty. But we feel the SVM results with single objects are encouraging. A more complete modeling of noise can be achieved by using both additive Gaussian noise and position noise within the same object. Testing of objects that have vertical, lateral, and orientation uncertainties all in some combination will be another future goal. Furthermore, we believe that if we more fully characterize the response of objects using a larger number of frequencies and possibly more  $B_k^j$ , the effect of vertical deviation noise may be lessened and the overall error rate may be decreased.

We also are in the process of retrieving and using the  $B_k^j$  from measurements of UXO and clutter objects in our classification process. Using these techniques and the four key distinguishing characteristics outlined at the beginning of this paper, we hope to establish a solid method to discriminate UXO from clutter.

## 9 Permeable Soil Studies

The second part of our research deals with the analysis of permeable soil. To accurately retrieve soil properties from measurements, we must fully examine the instrument we use. The GEM-3 sensor is manufactured by Geophex [28]. This instrument consists of two concentric, co-planar current loops in a bucking coil arrangement to generate a primary magnetic field. The secondary magnetic field is captured by the current generated on a pickup coil in the center of the instrument by  $\partial B/\partial t$ . The instrument reports this current in units that are proportional to the integral of magnetic flux over the receiver coil, normalized by the transmitted field as sampled by an additional coil within the sensor head. The instrument is proprietary, and all hardware is sealed within an outer casing. Very little can be said about the actual relationship between the true secondary fields and the measurements reported by the GEM-3. Furthermore, no study has been undertaken to cast or convert the data from the GEM-3 into the known units used within models. To understand why such a conversion ability is important, it is helpful to view the UXO problem from an inversion perspective. Machine learning techniques can make use of the modeled responses of a wide range of metallic objects to train a systematic discriminator that separates UXO from clutter objects on the basis of their EMI responses [30, 6]. To classify objects with measured data, previous studies normalized all measured and simulated data [6]. This

normalization creates a loss of valuable information about the magnitude of the response. However, if one were able to convert GEM-3 data into the units consistent with the modeled data, no information would be lost. Therefore, the recovery of this conversion relationship is a prerequisite for many types of advanced inversion studies. Another, possibly more basic, application is the inversion for soil properties. Given measurements of the soil response by the GEM-3, it would be possible to recover the soil’s susceptibility directly if one could translate the measurements into units of a modeled soil response.

Due to this need, this study was undertaken to characterize, through non-invasive means, the GEM-3 record of secondary field and how it relates to the modeled secondary field of objects. Furthermore, we also examined the significance of the discrete size of the GEM-3 receiver loop. Ultimately, with proper calibration, data in the GEM-3’s native units from magnetically responsive soil was used directly to infer broadband magnetic susceptibility.

## 10 Recovery of the Conversion Factor

Though the coil sizes of the GEM-3 are fixed, the current on the transmitter coils varies as a function of frequency. In essence the instrument normalizes all received fields relative to the strength of the transmitted field at each frequency. The instrument is not known to have any adaptive processing properties. Therefore, the relationship between the measured secondary field reported by the GEM-3 and any modeled response given the same loop geometries and an arbitrary assumed constant transmitter current would amount to a simple scaling factor. To recover this scaling factor, we used three metallic spheres to calibrate our modeled response to the GEM-3 measurements. This comparison between modeled response and measurements will determine the correct scaling factor.

### 10.1 Modeling of Metallic Spheres

We model metallic spheres as a special case of the spheroidal model. This model is well validated and produces EMI secondary field predictions for spheroidal objects with any conductivity and permeability values and in response to arbitrary excitation [2, 1, 5]. This model produces secondary field predictions in terms of A/m. The three specific objects that were modeled correspond to the measured metal spheres: steel, brass, and aluminum, all 3



Figure 6: Three metal spheres used in GEM-3 calibration. From left to right: brass, aluminum, and steel.

inches in diameter as shown in Figure 6.

## 10.2 Modeling of GEM 3 excitation field

The excitation field is generated by a analytical model that represents the GEM-3 instrument as a set of idealized wire loops. The transmitting sensor head consists of two current loops in series with radii of 20 cm and 11.074 cm. The smaller loop is placed concentrically inside the larger loop and serves as a bucking coil, approximately nulling the primary field at the center of the sensor head, where the receiver coil resides. There are 8 windings in the outer and 4 windings in the inner transmitter coil. We assume the wires in the transmitter coils carry 10 Amps. However, as mentioned earlier, this is not necessarily the true amount of current in use by the GEM-3. The recovered conversion factor will not convert GEM-3 measurements into the actual A/m units of the secondary field that was created during the measurement process. Rather, the factor will convert the measurements into the framework of our model. As long as we remain consistent in using the same model for the transmitter and receiver coils, the recovered conversion factor will always be valid.

We use the complete elliptical integral functions of the first and second kind to characterize the magnetic vector potential and vector field from a circular current loop in a cylindrical coordinate system. This calculation method is well established [24, 20, 17]. For a current loop of radius  $a$  and normal to the  $z$  axis in the  $z = z_o$  plane and with  $I_o$  current flowing in the  $\phi$  direction, the transverse and axial fields are,

$$B_r(r, \phi, z) = \frac{\mu_0 I_o}{2\pi} \frac{(z - z_o)}{r[(r + a)^2 + (z - z_o)^2]^{1/2}} \cdot \left[ -K(k_c) + \frac{r^2 + a^2 + (z - z_o)^2}{(r - a)^2 + (z - z_o)^2} E(k_c) \right] \quad (9)$$

$$B_z(r, \phi, z) = \frac{\mu_0 I_o}{2\pi[(r + a)^2 + (z - z_o)^2]^{1/2}} \cdot \left[ K(k_c) - \frac{r^2 - a^2 + (z - z_o)^2}{(r - a)^2 + (z - z_o)^2} E(k_c) \right], \quad (10)$$

where

$$k_c = \sqrt{\frac{4ar}{(r + a)^2 + (z - z_o)^2}}. \quad (11)$$

$K$  and  $E$  are the complete elliptical integral functions of the first and second kind, respectively. These equations will produce the primary magnetic fields at any position.  $(r, \phi, z)$  is the standard cylindrical coordinate system.

The excitation field is created from the superposition of two current loops that correspond to the two actual transmitting loops in the sensor head. Our model agrees with the alternative method of using numerical integration and application of Biot-Savart's Law but has the added benefit of being computationally more efficient.

### 10.3 Modeling of the Receiver Loop

Given the finite size of the receiver loop, the secondary field will not necessarily be uniform across the area of the loop. This is especially true if the object is close to the instrument. Therefore all modeled secondary fields are numerically integrated over the loop area to parallel the actual secondary field measurement. This integration is calculated by partitioning the loop area into segments of concentric rings. In our experience, over 300 divisions are needed for consistent results.

## 10.4 Measurements

Measurements were taken above each metal sphere by placing the GEM-3 instrument at points in a vertical grid. Horizontal spacing was in 2 cm increments from -30 cm to +30 cm from the position above the sphere. Vertical spacing was in 5cm increments from 13 cm to 28 cm above the surface of the sphere. The frequency range was from 30 Hz to 47 kHz. This wide range of measurement points both in space and frequency was taken to ensure that the recovered scaling factor is consistent: there must not be any variation due to object distance, frequency, or choice of target object. In other words, all the data must point to a scaling factor of the same value.

## 10.5 Matching Algorithm

We performed a dichotomy search within the range of possible values for the scaling factor and the sphere’s material properties to find the best match between the model’s prediction and the data. This search utilized the normalized mean square error as an objective function. This type of simple search is relatively fast but usually prone to getting stuck on local minima. In our investigation that difficulty was not encountered. The matching algorithm was independently repeated for the frequency response at each measurement point for each sphere. This method allows us to examine the results for consistency over space and frequency.

The main difficulty in the search algorithm was that the metallic spheres’ exact permeability and conductivity values were not precisely known. Therefore, to match the model’s EMI prediction with measurements, both the scaling factor and  $\mu$  and  $\sigma$  must be simultaneously recovered. As a simplification, the aluminum and brass spheres can be assumed to be non-permeable, and thus only their  $\sigma$  values and the scaling factor need to be recovered. Approximate values of sigma for these materials are available from standard textbooks, furnishing a reasonableness check. For the highly permeable steel sphere, only the ratio between  $\sigma$  and  $\mu$  affects the secondary response [23]. Therefore, relative  $\mu$  is assumed to be 100 and the normalized  $\sigma$  value is recovered along with the scaling factor.

Figure 7 shows the match between the modeled response and the measurement of the steel sphere. The match does extremely well save for the lowest and highest frequency points. We have observed that the GEM-3 can have difficulties capturing consistent responses at very low and very high EMI



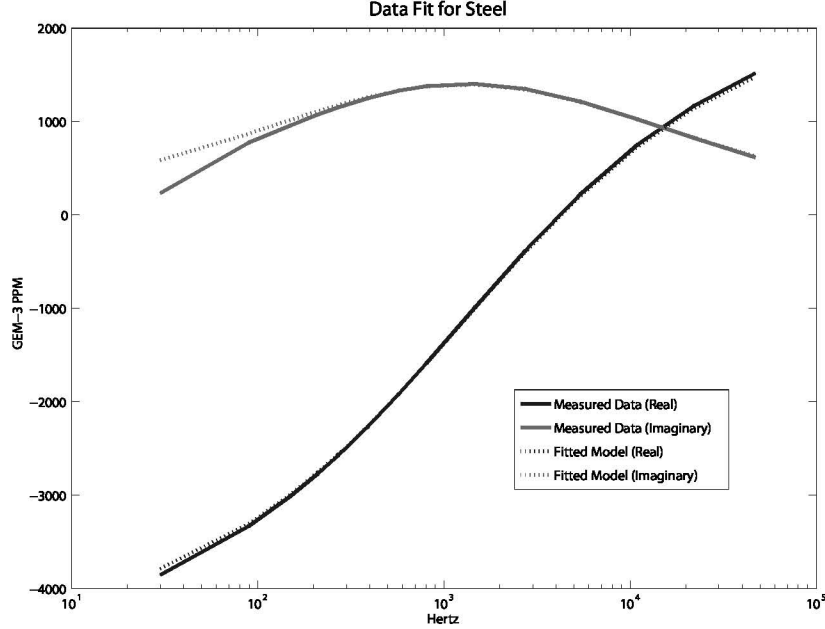


Figure 7: Figure showing the matching between model and measurement of a steel sphere at a single grid point.

frequencies. Therefore, the lowest and highest frequency data are ignored during the matching process.

## 11 Results

After performing this search, we average the scaling factors for all objects recovered at the closest 9 measurement points. We arrived at an overall value of  $4.93 \times 10^3$ . Division by this scalar will convert all GEM-3 measurements into the average magnetic field that would pass through the receiver coil within our model, given our specific transmitter loop.

Figure 8 plots the recovered conversion factors for the steel sphere as a function of position, assuming the GEM-3 is positioned at (0,0) on the axes. This analysis is useful because the scaling factor is assumed to be constant over space. Any radical departure from this phenomenology would signify that the matching algorithm of our forward model and the recovered scaling

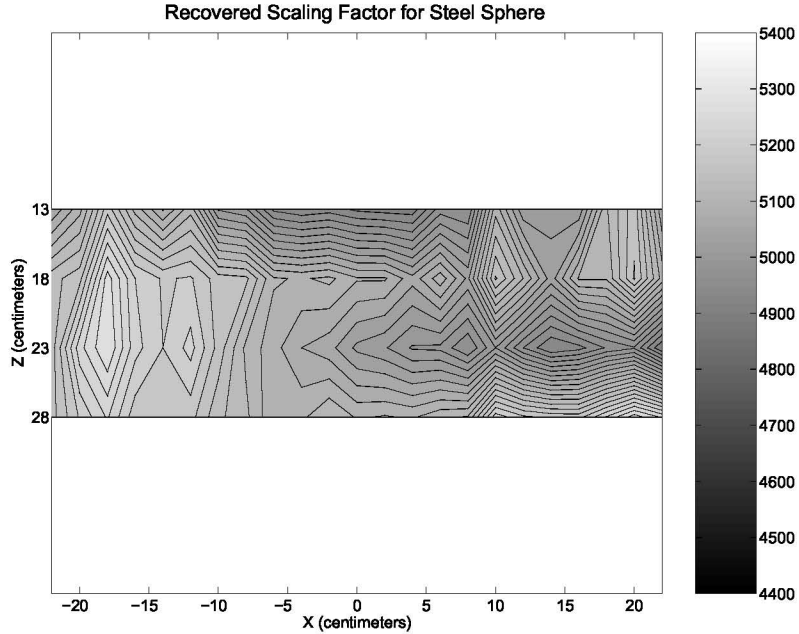


Figure 8: Plot of the retrieved conversion factor for the steel sphere as a function of position.

factor are incorrect.

Figure 8 as shown is not particularly illuminating, but all the data can be converted into a percent error from the averaged conversion factor of  $4.93 \times 10^3$ . This variation of the scaling factor can likewise be plotted over space. Shown in Figure 9 is the variation over space for the steel sphere. As the figure demonstrates, the variation is minimal with under 5% error. We see similarly good results for the brass and aluminum spheres shown in Figures 10 and 11, respectively.

## 12 Effect of Receiver Loop Size

If we can assume the secondary field is constant over the receiver loop, then it would be unnecessary to numerically integrate the fields within the loop area. This shortcut would save considerable computational time since the forward model would need to calculate only once per grid point as opposed to over

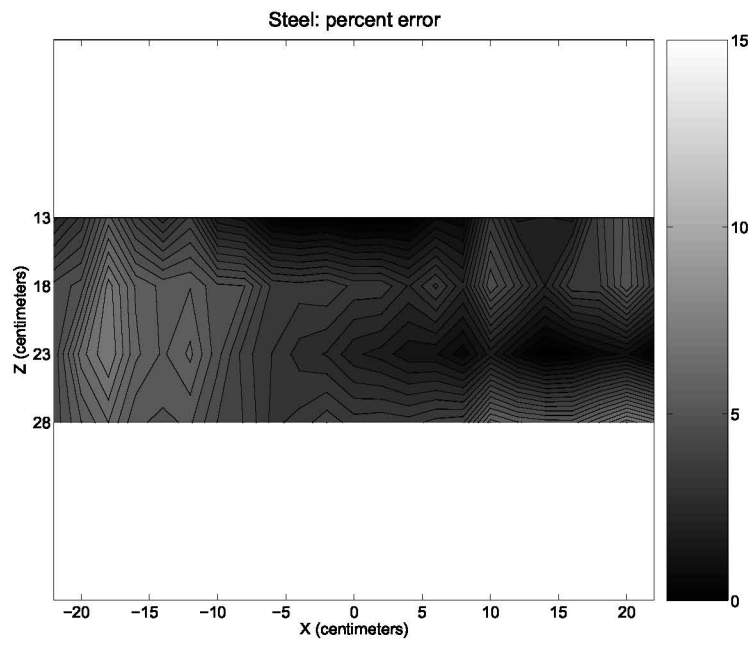


Figure 9: Plot of the variation of the retrieved conversion factor, as a percent error from  $4.93 \times 10^3$ , for the steel sphere as a function of position.

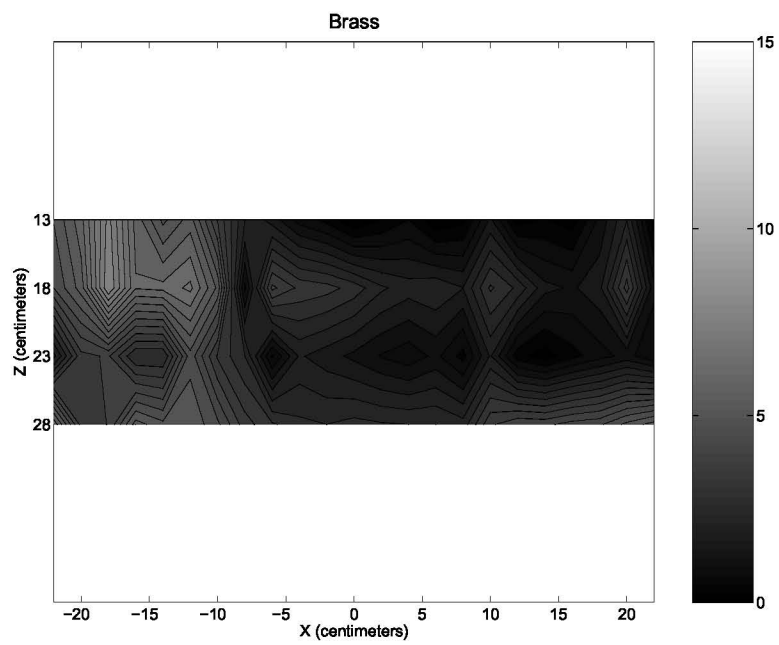


Figure 10: Plot of the variation of the retrieved conversion factor, as a percent error from  $4.93 \times 10^3$ , for the brass sphere as a function of position.

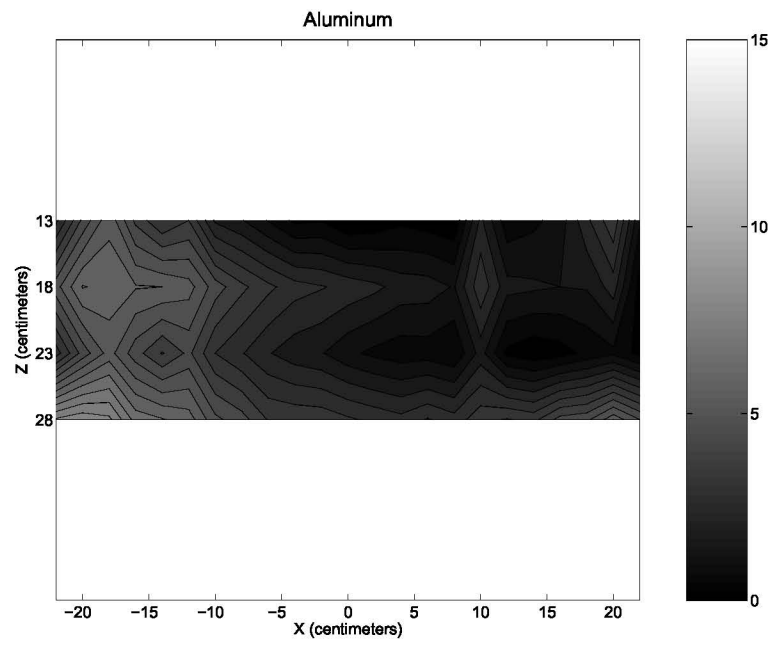


Figure 11: Plot of the variation of the retrieved conversion factor, as a percent error from  $4.93 \times 10^3$ , for the aluminum sphere as a function of position.

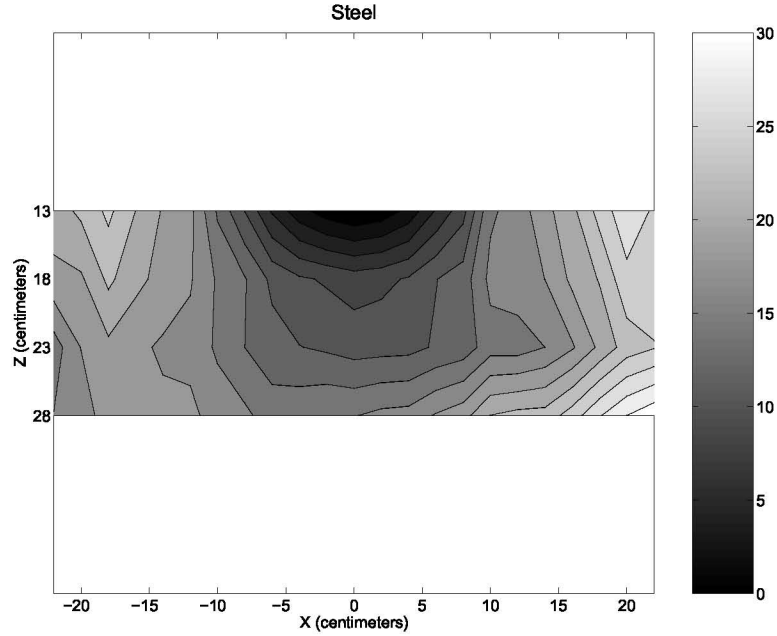


Figure 12: Plot of the variation of the retrieved conversion factor, as a percent error from  $4.24 \times 10^3$ , for the aluminum sphere as a function of position. No integration was performed over the receiver loop.

300 times per grid point. However, the secondary field is non-uniform across the receiver loop and has considerable implications on the recovery of the scaling factor. Shown in Figure 12 is data analogous to Figure 9 except that no numerical integration was performed over the receiver coil. The average magnetic field over the receiver loop was assumed to be the same as the field in the very center of the loop. Using this method, a new scaling factor, averaged from the closest 9 measurement points, was obtained:  $4.24 \times 10^3$ . Since the figure shows considerable spatial variation of the scaling factor from the averaged value, we conclude that numerically integrating the fields within the receiver loop is necessary.

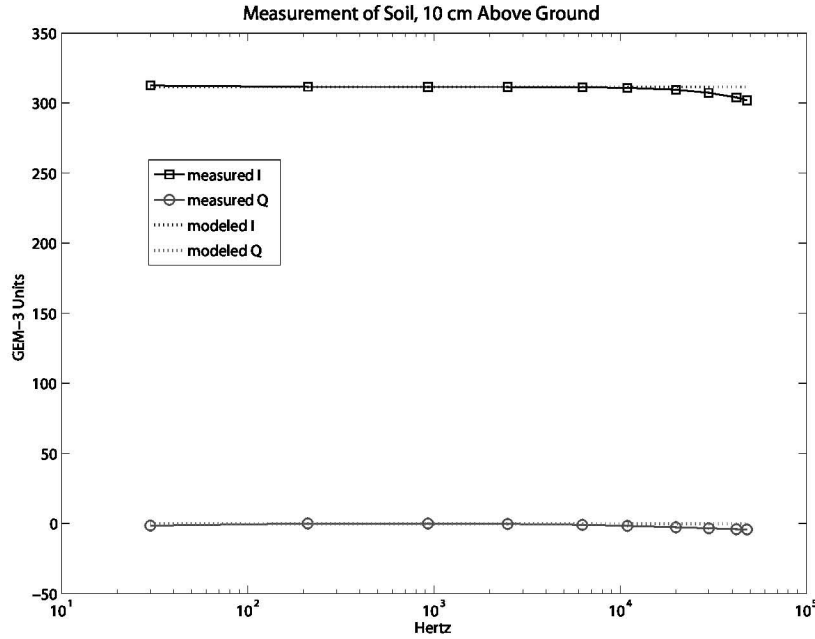


Figure 13: Comparison between measured inphase (I) and quadrature (Q) ground response and prediction using half space soil model with an applied scaling factor.

## 13 Validation and Application of the Scaling Factor

Given the scaling factor, we would like to check how reasonable it is. The solid curves in Figure 13 show in the Inphase and Quadrature response of a sample of soil when the GEM-3 is 10 cm above the surface. We implemented a half-space model of permeable soil. The d.c. soil susceptibility value was adjusted until we found the best match,  $\chi_0 = 2.52 \times 10^{-3}$ . This value is solidly within the range of reasonable soil values as reported by others [19, 25].

## 14 Conclusion and Discussion

This study focused on characterizing GEM-3 measurements and how they related to modeled quantities. Our techniques to recover the scaling factor

can be applied to any other model of the GEM-3 and many other EMI sensors as well. We have already begun characterizing the newest EMI instrument by Geophex, the vector GEM-3D+, in this manner. Furthermore, we have found that the finite size of the receiver loop must be taken into account when examining the GEM-3 and relating it to model data. We have shown that without numerically integrating over the receiver loop area, the retrieved scaling factor is incorrect. This need for integrating may have significant implications for future work in inversion studies.

Lastly, we used our retrieved scaling factor to match the modeled response of permeable, susceptible soil to measurements of soil and have found reasonable soil susceptibility values. This not only demonstrates the validity of our scaling factor but also points to the possibility of characterizing soil from GEM-3 measurements alone and avoiding the need to conduct laboratory analysis on core samples outside of in situ conditions.

Instruments in the GEM series effectively measure an MQS coefficient, being a ratio of some measure of received to some measure of transmitted field. In wave phenomena this would be a kind of reflection coefficient. In the MQS regime it is better called a response coefficient. The calibration performed here translate the response coefficient obtained in the instrument's native units into one that can be applied more generally, as in our susceptibility inferences. Given a knowledge of transmitter geometry and current, one can use the same methodology to go further and translate data into actual the A/m received field values. We are currently doing this in application to a newly developed time-domain instrument.

## References

- [1] C. O. Ao. *Electromagnetic Wave Scattering by Discrete Random Media with Remote Sensing Application*. PhD thesis, Massachusetts Institute of Technology, January 2001.
- [2] B. E. Barrowes. *Electromagnetic Scattering and Induction Models for Spheroidal Geometries*. PhD thesis, Massachusetts Institute of Technology, January 2004.
- [3] T. H. Bell, B. J. Barrow, and J. T. Miller. Subsurface discrimination using electromagnetic induction sensors. *IEEE Trans. on Geoscience and Remote Sensing*, 39(6):1286–1293, June 2001.



- [4] C. Bishop. *Neural Networks for Pattern Recognition*. Clarendon Press, 1995.
- [5] H. Braunisch. *Methods in Wave Propagation and Scattering*. PhD thesis, Massachusetts Institute of Technology, February 2001.
- [6] X. Chen. *Inverse Problems in Electromagnetic*. PhD thesis, Massachusetts Institute of Technology, May 2005.
- [7] X. Chen, K. O'Neill, T. M. Grzegorzcyk, and J. A. Kong. Spheroidal mode approach for the characterization of metallic objects using electromagnetic induction. *IEEE Trans. on Geoscience and Remote Sensing*, 45(3):697–706, March 2007.
- [8] L. Collins, P. Gao, and L. Carin. An improved bayesian decision theoretic approach for land mine detection. *IEEE Trans. on Geoscience and Remote Sensing*, 37:811–819, March 1998 1998.
- [9] L. Collins, P. Gao, D. Schofield, J. Moulton, L. C. M. abd D. M. Reidy, and R. C. Weaver. A statistical approach to landmine detection using broadband electromagnetic induction data. *IEEE Trans. on Geoscience and Remote Sensing*, 40:950–962, April 2002.
- [10] L. Collins, Y. Zhang, J. Li, H. Wang, L. Carin, S. J. Hart, S. L. Rose-Pehrsson, H. H. Nelson, and J. R. McDonald. A comparision of the performance of statistical and fuzzy algorithms for unexploded ordnance detection. *IEEE Trans. on Fuzzy Systems*, 9:17–30, February 2001.
- [11] P. Gader, H. Frigui, G. Vaillette, B. Nelson, and J. Keller. New results in fuzzy set based detection of landmines with GPR. Detection and Remediation Technologies for Mines and Minelike Targets IV Conf. Int. Symp. Aerospace/Defense Sensing and Controls, April 1999.
- [12] P. Gao, L. Collins, P. Garber, N. Geng, and L. Carin. Classification of landmine-like metal targets using wideband electromagnetic induction. *IEEE Trans. on Geoscience and Remote Sensing*, 38:1352–1361, May 2000.
- [13] N. Geng, K. E. Baum, and L. Carin. On the low frequency natural responses of conducting and permeable targets. *IEEE Trans. on Geoscience and Remote Sensing*, 37:347–359, January 1999.

- [14] D. Keiswetter, I. J. Won, B. Barrow, and T. Bell. Object identification using multi-frequency EMI data. In *Proc. UXO Forum*. 1999.
- [15] M. Raza, I. Gondal, D. Green, and R. L. Coppel. Feature selection and classification of gene expression profile in hereditary breast cancer. In *Hybrid Intelligent Systems*, pages 315–320. IEEE Computer Society, 2004.
- [16] S. Ruping. *mySVM-Manual*. University of Dortmund, Lehrstuhl Informatik 8 edition, 2000. <http://www-ai.cs.uni-dortmund.de/SOFTWARE/MYSVM/index.html>.
- [17] R. A. Schill Jr. General relation for the vector magnetic field of a circular current loop: A closer look. *IEEE Transactions on Magnetism*, 39(2):961–967, March 2003.
- [18] F. Shubitidze, K. O’Neill, K. Sun, I. Shamatava, and K. D. Paulsen. A hybrid full MAS and combined MAS/TSA algorithm for electromagnetic induction sensing. volume 19, pages 112–126. ACES(Applied Computational Electromagnetics Society) Journal, 2004.
- [19] J. E. Simms, R. L. Van Dam, and J. M. H. Hendrickx. Classification of magnetic susceptibility anomalies and their relevance to uxo detection. *FastTIMES*, 10(2):48–51, 2005.
- [20] W. R. Smythe. *Static and Dynamic Electricity*. McGraw-Hill, 3rd edition, 1968.
- [21] K. Sun, K. O’Neill, L. Liu, F. Shubitidze, I. Shamatava, and K. D. Paulsen. Analytical solutions for EMI scattering from general spheroids with application in signal inversion for UXO identification. volume 5089 of *Detection and Remediation Technologies for Mines and Minelike Targets VIII*. SPIE, April 2003.
- [22] K. Sun, K. O’Neill, I. Shamatava, and F. Shubitidze. Application of prolate spheroid solutions in simulation of EMI scattering with realistic sensors and objects. pages 531–537. Applied Computational Electromagnetics (ACES), March 2003.

- [23] K. Sun, K. O'Neill, F. Shubitidze, I. Shamatava, and K. D. Paulsen. Fast data-derived fundamental spheroidal excitation models with application to UXO discrimination. *IEEE Trans. on Geoscience and Remote Sensing*, 43:2573–2583, November 2005.
- [24] J. van Bladel. *Electromagnetic Fields*. Hemisphere Pub. Corp., 1985.
- [25] R. L. van Dam, J. M. H. Hendrickx, and B. e. a. Harrison. Spatial variability of magnetic soil properties. *SPIE: Detection and Remediation Technologies for Mines and Minelike Targets IX*, 5415, 2004.
- [26] V. Vapnik. *Statistical Learning Theory*. Wiley, 1998.
- [27] P. H. Winston. *Artificial Intelligence*. Addison-Wesley, 1993.
- [28] I. J. Won, D. A. Keiswetter, and D. R. Hansen. GEM-3: A monostatic broadband electromagnetic induction sensor. *J. Environ. Eng. Geophys.*, 2:53–64, 1999.
- [29] B. Zhang, K. O'Neill, T. M. Grzegorzczuk, and J. A. Kong. Environmental effects on UWB electromagnetic induction inversion techniques and forward modeling of unexploded ordnance. page 127, Cambridge, Massachusetts, March 2006. Progress in Electromagnetic Research Symposium (PIERS).
- [30] B. Zhang, K. O'Neill, T. M. Grzegorzczuk, and J. A. Kong. Use of EMI response coefficients from spheroidal excitation and scattering modes to classify objects via SVM. volume 6217. SPIE, April 2006.